Available online at www.sciencedirect.com
SCIENCE DIRECT®
ELSEVIER
Ultramicroscopy 104 (2005) 126–140
ultramicroscopy
www.elsevier.com/locate/ultramic

Modelling imaging based on core-loss spectroscopy in scanning transmission electron microscopy

S.D. Findlay[a], M.P. Oxley[a], S.J. Pennycook[b], L.J. Allen[a,*]

[a]*School of Physics, University of Melbourne, Victoria 3010, Australia*
[b]*Condensed Matter Sciences Division, Oak Ridge National Laboratory, P.O. Box 2008, Oak Ridge, TN 37831-6030, USA*

Received 30 November 2004; received in revised form 14 February 2005; accepted 2 March 2005

Abstract

Recent experimental realizations of atomic column resolution core-loss spectroscopy in the scanning transmission electron microscope have increased the importance of routinely modelling core-loss images. We discuss different approaches to wave function simulation and how they may be used in conjunction with the mixed dynamic form factor model to simulate images resulting from such inelastic scattering events. It is shown that, as resolution improves and in situations where the degree of thermal scattering is high, detailed quantitative comparisons will require the thermal scattering of electrons to be adequately modelled. Indeed, for sufficiently strong thermal scattering even qualitative interpretation may be affected: we give an example where this leads to a contrast reversal. We describe two methods suited to this purpose, the frozen lattice model and the scattering factor model, and explain how they may be combined with the mixed dynamic form factor approach.
© 2005 Elsevier B.V. All rights reserved.

PACS: 61.14−x; 61.85.+p; 68.37Lp

Keywords: Scanning transmission electron microscopy; Core-loss spectroscopy; Frozen lattice model; Mixed dynamic form factor

1. Introduction

The steadily improving image resolution in scanning transmission electron microscopy (STEM), made possible by the development of aberration correctors [1], will soon allow atomic resolution electron energy loss spectroscopy (EELS) based on core-loss events to be performed routinely. However using equipment with the necessary sensitivity does not ensure that the images will be directly interpretable. A long standing question is whether signals arising from core-loss events are sufficiently localized that EELS images can be visually interpreted column-by-column in the manner often applied to high-angle annular dark field images. Recent papers, combining theoretical simulations and experimental

*Corresponding author. Tel.: +61 3 8344 7402; fax: +61 3 9347 4783.
E-mail address: lja@physics.unimelb.edu.au (L.J. Allen).

0304-3991/$ - see front matter © 2005 Elsevier B.V. All rights reserved.
doi:10.1016/j.ultramic.2005.03.004

results, demonstrate that this is indeed possible [2–4]. Those papers emphasized both the importance of being able to simulate core-loss images in the planning and interpretation of experiments and the further insights which might be gained by quantitative comparison between theory and experiment.

We shall discuss an approach to the calculation of inelastic images based upon mixed dynamic form factors (MDFFs) [5–15]. Such image simulation involves combining the MDFFs with the wave function describing the electron prior to the core-loss event. Allen and co-workers have recently described methods for using MDFFs to simulate core-loss spectroscopic images in STEM using either Bloch wave or multislice methods [16–18]. In these calculations an absorption resulting from the thermal motion of the crystal was included in the determination of the elastic wave function. For fine probes, such as current and next generation equipment seek to provide, this absorption causes significant attenuation of the elastic wave function. It is therefore important to quantify the extent to which the effectively absorbed electrons also contribute to EELS images in STEM. The method we previously proposed for doing this [2,16] is inadequate for atomic-scale STEM probes.

A popular method for dealing with the detailed spatial distribution of scattered electrons, which accounts for the thermal motion of the atoms, is the frozen lattice or frozen phonon model [19–24]. We present a synthesis of the MDFF method and the frozen lattice model. We also present synthesis between the MDFF method and a variant on the scattering function model of Anstis and co-workers [25,26], in a form which relates it to the models of Rose and co-workers [27–30].

2. Absorptive models

Both the Bloch wave and multislice MDFF simulation methods of Allen and co-workers [16–18] are based upon a cross-section expression for inelastic scattering [5–11]. This expression gives the image resulting from some particular scattering mechanism—inner-shell ionization, say—arising from the electron distribution described by a wave function.

As given by Allen and co-workers [16], the cross-section expression, as a function of probe position $\mathbf{R}$ and crystal thickness t and written in a form amenable to evaluation via multislice methods, is

$$\begin{aligned}\sigma(\mathbf{R},t) &= \sigma_{\mathrm{dyn}}(\mathbf{R},t)+\sigma_{\mathrm{diff}}(\mathbf{R},t)\\ &= \frac{1}{A}\int_0^t\left[\sum_{\mathbf{g},\mathbf{h}}\mu_{\mathbf{h},\mathbf{g}}(z)\Psi^*(\mathbf{R},\mathbf{h},z)\Psi(\mathbf{R},\mathbf{g},z)\right]\mathrm{d}z\\ &\quad+\left[V-\int_0^t\int_A|\psi(\mathbf{R},\mathbf{r}_\perp,z)|^2\,\mathrm{d}\mathbf{r}_\perp\,\mathrm{d}z\right]\mu_{\mathbf{0},\mathbf{0}}(z),\end{aligned} \tag{1}$$

where

$$\Psi(\mathbf{R},\mathbf{h},z)\equiv\int_A\psi(\mathbf{R},\mathbf{r}_\perp,z)\mathrm{e}^{-2\pi\mathrm{i}\mathbf{h}\cdot\mathbf{r}_\perp}\,\mathrm{d}\mathbf{r}_\perp, \tag{2}$$

$(\mathbf{r}_\perp,z)$ are the spatial coordinates within the crystal with the z-direction coincident with the optical axis, $\mathbf{h}$ and $\mathbf{g}$ denote reciprocal space vectors, and $\psi(\mathbf{R},\mathbf{r}_\perp,z)$ denotes the wave function in real space with two-dimensional (2D) Fourier transform $\Psi(\mathbf{R},\mathbf{h},z)$. The elements $\mu_{\mathbf{h},\mathbf{g}}(z)$ are the MDFFs and contain the details of both the inelastic interaction and the detector geometry. Expressions for the MDFFs for core-loss excitation may be found in Refs. [8,10,16]. The z dependence indicates that one may use different $\mu_{\mathbf{h},\mathbf{g}}$ elements at different depths if a projected potential approximation cannot be invoked. The factors containing specimen area A and volume V are present for normalization. In the absorptive model the wave function $\psi(\mathbf{R},\mathbf{r}_\perp,z)$ in Eq. (1) is the elastic wave function attenuated by the absorptive potential which, following the approach of Hall and Hirsch [31], accounts for scattering away from the Bragg peaks.

We have retained the notation and terminology of earlier derivations [9], where Eq. (1) defines a cross section. However the images recorded in STEM are most readily quantified as a fraction of the incident current. This is accomplished simply by dividing the cross section by the effective incident area A. The result is that STEM plots throughout this paper are labelled as fractional intensity, expressing the fraction of the incident current that makes up the measured intensity.

The cross-section expression above is given as the sum of two parts. The first is the dynamical contribution, $\sigma_{\mathrm{dyn}}(\mathbf{R}, t)$, which gives the image obtained when the general cross-section expression is applied to the wave function describing elastic scattering, which is to say the contribution to the signal from ionization events caused by electrons in the elastic wave function. The second, $\sigma_{\mathrm{diff}}(\mathbf{R}, t)$, called the diffuse term, results from the sum over the images obtained when the general cross-section expression is applied to the mutually incoherent plane waves presumed to describe the electrons absorbed by thermal scattering [9], which is to say the contribution to the signal from ionization events caused by electrons which have already undergone inelastic thermal scattering.

In conventional transmission electron microscopy, the cross-section expression has been shown to accurately simulate channelling maps [11–14]. In that context the contribution from thermally scattered electrons was essential in obtaining excellent agreement with experiment. The diffuse contribution is effectively modelled as the product of an average ionization probability and the proportion of electrons which had undergone thermal scattering. Such an approach must ultimately fail when localized probes are used; in the extreme case of a spectroscopic signal deriving from a localized impurity we do not expect an EELS signal to result when the probe is far away from the impurity, irrespective of the amount of absorption due to thermal scattering.

For the purposes of qualitative comparison with EELS images one might consider solely the dynamical contribution in Eq. (1). However for quantitative comparison it will prove necessary to take thermally scattered electrons into account when the degree of absorption is significant. The diffuse contribution to the image in the form described above, which was very successful in the case of plane wave illumination, shall be seen to be inadequate in STEM when fine probes are used. We will present two methods which can calculate the contribution which the diffuse term was meant to embody.

We will refer to the model in which both the dynamical and diffuse contributions in Eq. (1) are used to simulate an image as the absorptive model since it is to be evaluated using absorption via an Einstein model. The dynamical contribution alone is a useful reference, and we will refer to the model evaluated using absorptive code but neglecting the diffuse term as the dynamical model. We will explore two additional methods to account for thermal scattering. The first is the frozen lattice model, the second is the scattering function model. To make fair comparisons we shall use the multislice method to evaluate all the models.

3. The frozen lattice MDFF synthesis

The frozen lattice method [19–23], also referred to as the frozen phonon method, is based on the fact that the time scale of an electron traversing the crystal is orders of magnitude smaller than the average vibrational period of atoms in the specimen. Any given electron is therefore effectively influenced by a static potential distribution in which the atoms are displaced from their equilibrium positions in accordance with the phonon modes present. These displacements break the perfect periodicity. In the case of plane wave incidence this leads to non-zero intensity between the Bragg spots. The result of any given experiment is the average over many frozen configurations. No absorption is used here: for a single configuration we define an elastic wave function containing all the electron density.

To adapt the cross-section approach to the frozen lattice method we define the total cross section as an average over the cross sections for many configurations. We denote the different configurations by index n, the wave function within a crystal in the nth configuration by $\psi_n(\mathbf{R}, \mathbf{r}_\perp, z)$, and the MDFFs appropriate to that configuration by $\mu^n_{\mathbf{h},\mathbf{g}}(z)$. Thus

$$\begin{aligned}\sigma(\mathbf{R}, t) &= \frac{1}{N}\sum_{n=1}^{N}\sigma_n(\mathbf{R}, t)\\ &= \frac{1}{AN}\sum_{n=1}^{N}\int_0^t\left[\sum_{\mathbf{g},\mathbf{h}}\mu^n_{\mathbf{h},\mathbf{g}}(z)\Psi^*_n(\mathbf{R}, \mathbf{h}, z)\right.\\ &\quad\left.\times\Psi_n(\mathbf{R}, \mathbf{g}, z)\right]\mathrm{d}z, \qquad (3)\end{aligned}$$

in which N denotes the number of different configurations used, $\Psi_n(\mathbf{R},\mathbf{h},z)$ is calculated from $\psi_n(\mathbf{R},\mathbf{r}_\perp,z)$ via Eq. (2), and the cross sections have the form of the dynamical term in Eq. (1) because for a given frozen lattice all the scattering is coherent. In analogy to the elastic potential in the frozen lattice model, the MDFFs should contain site terms modified for the atom displacements but should not contain Debye–Waller factors. The computation is performed on a supercell, in order to adequately sample both real and reciprocal space and so propagate a convergent probe, and the site terms accommodate different static displacements in the different cells of which the supercell is comprised thus accounting for frozen phonon modes through the crystal.

To make the calculations tractable we make an approximation. Many more Fourier coefficients are required to describe the non-periodic potential of the frozen lattice model than to describe the periodic potential of an absorptive calculation, both for the elastic potential and for the MDFF elements. In the latter case this is problematic: calculating $\mu_{\mathbf{h},\mathbf{g}}(z)$ is computationally intensive. The lack of periodicity also removes the block-diagonal property whereby $\mu^n_{\mathbf{h},\mathbf{g}}(z)$ is only non-zero if $\mathbf{h}$–$\mathbf{g}$ is a physical reciprocal lattice vector [17]. We will suggest one means by which this simplifying property, the periodicity, may be regained for the MDFF elements.

This simplification supposes we may add Debye–Waller factors to the MDFFs as an alterative to using the atomic displacements. To justify this approximation we reason as follows. Let us neglect correlations; we will use an Einstein model. The change in the wave function incident upon any given slice due to the elastic scattering within this slice is small. In calculating the contribution to the EELS signal from said slice it is therefore sufficient to use the wave function from the previous slice. Having neglected correlations, this wave function is completely independent of whatever position might be assigned to the atoms in the present slice. The dissociation at each and every slice between the wave function at that slice and the MDFFs to be used for that slice allows the configurational average over these quantities to be performed separately. Eq. (3) may thus be approximated by

$$\sigma_{\mathrm{dyn}}(\mathbf{R},t) = \frac{1}{AN}\sum_{n=1}^{N}\int_0^t \left\{ \sum_{\mathbf{g},\mathbf{h}} \mu_{\mathbf{h},\mathbf{g}}(z) \times \Psi_n^*(\mathbf{R},\mathbf{h},z)\Psi_n(\mathbf{R},\mathbf{g},z) \right\} \mathrm{d}z, \tag{4}$$

where the $\mu_{\mathbf{h},\mathbf{g}}(z)$ elements now contain Debye–Waller factors. We have numerically tested this approximation and found it to be justified. Note that while using Debye–Waller factors is sufficient for the MDFFs describing core-loss events, it is insufficient for describing the thermally scattered electrons, hence the use of the frozen lattice model.

By way of example let us consider a 100 Å thick slab of silver viewed along the [0 0 1] zone axis from which EELS line scans along the [1 0 0] shall be taken using a 100 keV aberration-balanced probe characterized by defocus $\Delta f = 62$ Å, third-order spherical aberration $C_s = -0.05$ mm, fifth-order spherical aberration $C_5 = 63$ mm, and probe-forming semi-angle of 20 mrad. The EELS signals will be integrated over a detector semi-angle of 20 mrad and energy window of 40 eV above ionization threshold. Figs. 1(a) and (b) show line scans for the Ag M-shell, with edge at 395 eV, and L-shell, with edge at 3.5 keV, respectively. The former is more accessible experimentally than the latter. Plots are shown for the dynamical model including absorption, the dynamical model without absorption and for the frozen lattice MDFF synthesis.

Comparing the dynamical results with those using the frozen lattice model, we see the sort of differences anticipated: the signal using the frozen phonon model is slightly higher due to the contribution of the thermally scattered electrons, and more so about column locations where the degree of absorption is greater. However it is the shape of the M-shell plot which is most striking, because the peaks are not on the columns, as they are for the L-shell, but rather are between them.

This surprising prediction is a result of thermal scattering and absorption. One way to show this is to simulate the dynamical contribution without absorption, and the relevant plot in Fig. 1(a) shows that for such a model case the peaks would,

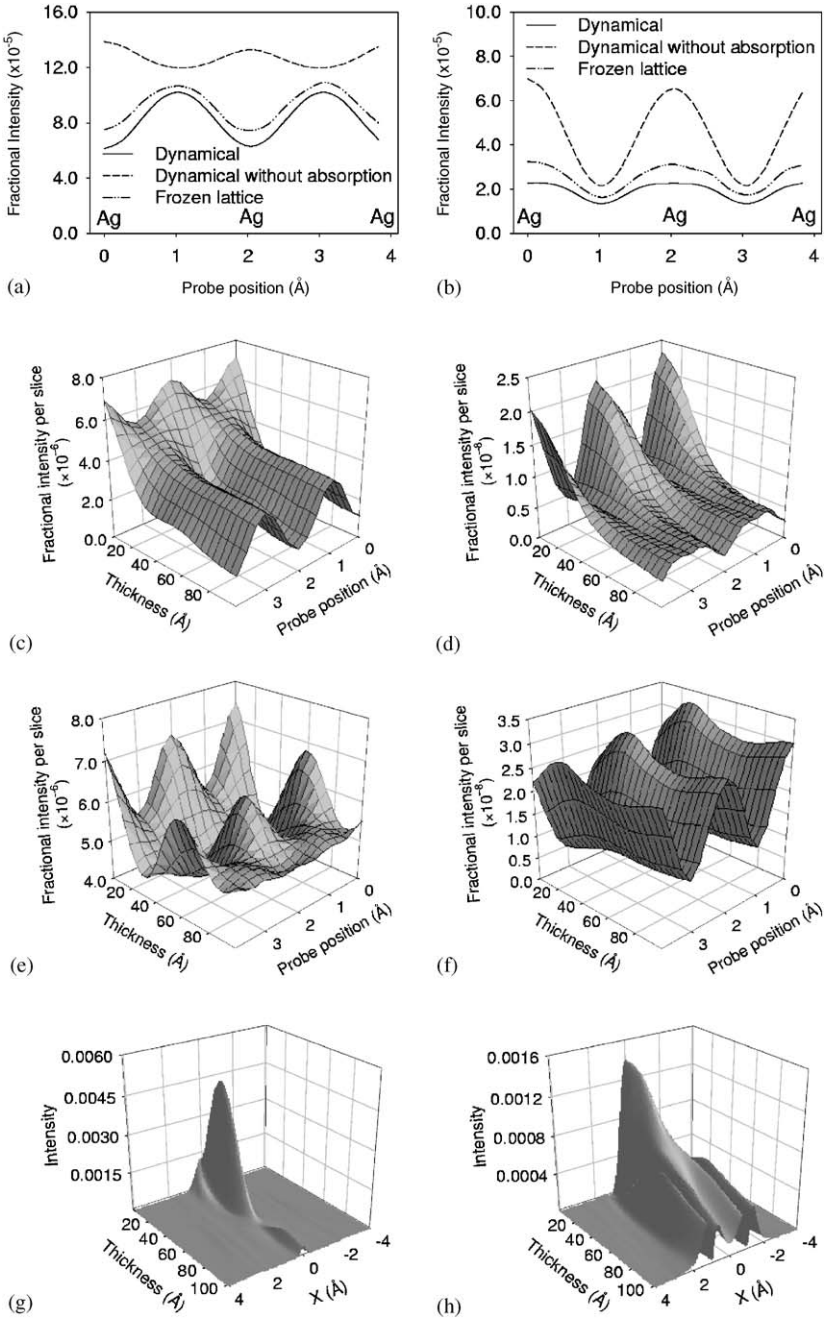

Fig. 1. EELS line scans for Ag (a) M-shell and (b) L-shell using the dynamical model [i.e. using only the first term in Eq. (1)], the dynamical model without absorption, and the frozen lattice model. (c) and (d) show the contributions per slice for the M- and L-shell results, respectively, using the dynamical model. (e) and (f) show the contributions per slice for the M- and L-shell results, respectively, using the dynamical model without absorption. (g) and (h) show intensity plots across the wavefunction as a function of depth for the probe on the Ag column and on the gap between the columns, respectively.

more intuitively, appear on the columns. The mechanism bringing this about is made more clear in Figs. 1(c) and (d), which show the contribution per slice in the dynamical model including absorption, and (e) and (f), which show the contribution per slice in the dynamical model excluding absorption. Figs. 1(c) and (d) show that for the first few layers the contribution has a shape well-representing the atom locations. However as the thickness increases, the signal strength on the heavy Ag columns is increasingly attenuated while the signal strength in the gap between the columns is not much affected. In the M-shell image this leads to the integrated signal from the gap being greater than that on the Ag columns. In the L-shell case, the integrated signal has not yet lead to a reversal in contrast, though when the calculation is carried out to 200 Å a similar effect is observed. Figs. 1(e) and (f) show a more sustained, though oscillating, contribution to the signal in the absence of absorption, and comparison with Figs. 1(c) and (d) show the regions in which absorption has most affected the contribution. Figs. 1(g) and (h) show the intensity along the [1 0 0] line between the atoms for the probe positioned on the Ag column and on the gap between columns, respectively. The dramatic reduction of intensity of the probe on the column within the first 50 Å is apparent. For the probe over the gap we see some spreading of the probe towards neighbouring columns. While the electron density reaching the column is attenuated, the continuing dispersal from the probe location is able to sustain a signal. It should be noted too that the interaction region in which M-shell ionization occurs is more delocalized and thus a greater contribution is to be expected with the probe displaced somewhat from the column than for the L-shell case.

The M-shell result demonstrates the importance of appreciating the role of absorption. The prediction is eminently testable, say through comparison of contrast in simultaneously acquired EELS and high-angle annular dark field images. However because of the unexpected form of the M-shell results, whereby the peaks do not coincide with the columns, we shall take the case of the L-shell EELS image in our subsequent testing of the algorithms, even though the energy loss involved makes it unsuitable for standard detectors.

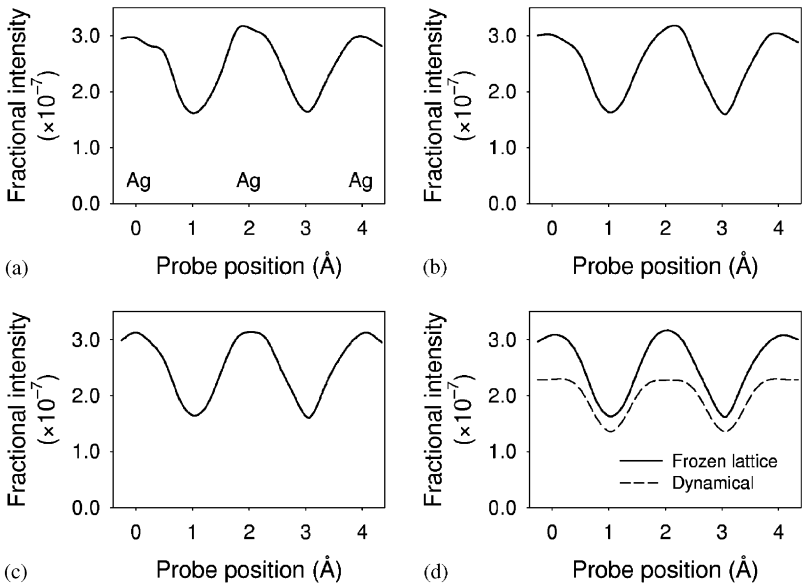

Fig. 2. Ag L-shell EELS line scans in Ag using the aberration-balanced probe. The zone axis is [0 0 1], the scan is along [1 0 0]. The accelerating voltage is 100 kV. The crystal thickness is 100 Å. The average is taken over (a) five configurations, (b) 10 configurations, (c) 15 configurations, and (d) 20 configurations. The final image includes a dynamical model calculation for comparison.

For simulating diffraction patterns via the frozen lattice model, an average over 20 or so configurations is required for good convergence [21,22]. For high-angle annular dark field imaging, which integrates over much of the fine detail, this number may be reduced. How many configurations are required for adequate convergence in simulating EELS images? Appreciably under-converged calculations reveal themselves through some irregularity which is inconsistent with expectations of symmetry and smoothness, though the converse—that symmetry and smoothness indicate adequate convergence—is not guaranteed. That said, the inelastic images depend most strongly on the low order Fourier coefficients of the wave function, and as such the results are not exquisitely sensitive to the finest features of the electron density.

Fig. 2 indicates the degree of convergence obtained as the number of configurations in the average increases. It is seen that irregularities persist in the result for 10 configurations, but have been essentially removed by 15–20. Fig. 2(d) shows both frozen lattice and dynamical calculations, demonstrating the importance of accounting for the thermal scattering: for a 100 Å thick silver sample almost a third of the signal strength is attributable to ionization events caused by electrons which have, in the dynamical model, been absorbed.

4. The scattering function MDFF synthesis

The frozen lattice model provides an intuitive picture of scattering from a crystal in thermal motion. It is able to accommodate any model for the phonon dispersion curve which describes possible atomic configurations in the crystal. It also makes significant demands on computation time, via the average over many configurations, and possesses stringent conditions for convergence, via the use of sharp (cf. thermally smeared) scattering potentials.

A model in which some of the averaging is accomplished analytically may offer some advantages in terms of computation time. The scattering function approach of Anstis and co-workers [25,26] is one such method: the effect of transmission through a phase grating was analytically averaged over the probability distribution of atom positions. They showed that the transmitted density could be expressed as the incoherent sum of several wave functions, the so-called scattering functions of the atom. In full detail this approach would be equivalent to a frozen lattice calculation, however we shall use a simplified model in which we apply the average to a kinematic model rather than a phase grating model. The reason for this is two-fold. Firstly it relates directly to the model of Hall and Hirsch [31] upon which the majority of absorptive potential calculations are based (though Anstis has presented modified scattering factors for the more elaborate phase grating approach [32]). Secondly it will be seen that the resultant first-order terms are precisely those of the generalized multislice formulation of Rose and co-workers [27–30], allowing a further useful comparison of models.

Hall and Hirsch [31] used reasoning similar to that underpinning the later frozen lattice model to obtain the absorption potential in the Einstein model. They derived, in a kinematic approximation, an expression for the intensity of the diffracted wave field arising from a lattice and performed the average over phonon modes analytically. Their approach identifies a contribution to the scattered intensity which derives from the Debye–Waller factor averaged projected potential, but groups the remainder together to be treated as an absorption. In a phase grating formulation Anstis took this approach further to obtain a description of the total intensity distribution as the sum of scattering functions [25]. In the Appendix we retain the kinematic approximation of Hall and Hirsch but use the concept of Anstis and co-workers to express the result in terms of mutually incoherent scattering functions. These functions all have the form of a product of an incident wave field and an effective scattering potential. The key result is that the scattered intensity from a single atom may be expressed as

$$\langle I(\mathbf{s})\rangle = \sum_{n=0}^{\infty}\sum_{k=0}^{n} |\mathscr{F}\{V_{n,k}(\mathbf{r}_\perp)\psi(\mathbf{r}_\perp)\}|^2, \tag{5}$$

where $\langle \ldots \rangle$ denotes the thermal average taken in an Einstein model, $\mathscr{F}$ denotes the 2D Fourier transform, $\psi(\mathbf{r}_\perp)$ is the wave function incident upon the atom,

$$V_{n,k}(\mathbf{r}_\perp) \equiv A_{n,k} \sum_{\mathbf{h}} f_{\mathbf{h}} \exp[-M(\mathbf{h})] h_x^k h_y^{n-k} \times \exp[2\pi i \mathbf{h} \cdot (\mathbf{r}_\perp - \mathbf{R}_0)] \quad (6)$$

with elastic scattering factor $f_{\mathbf{h}}$, Debye–Waller factor $M(\mathbf{h}) = 2\pi^2 \langle u_p^2 \rangle \mathbf{h}^2$ for projected mean square displacement $\langle u_p^2 \rangle$, $\mathbf{R}_0$ the mean atom position, and

$$A_{n,k} = \sqrt{\frac{[4\pi^2 \langle u_p^2 \rangle]^n}{(n-k)!k!}}. \quad (7)$$

Eq. (5) shows that the intensity is made up of an incoherent sum of terms which individually have the form of scattered wave functions. Note that the potential in the zeroth-order term, $V_{0,0}(\mathbf{r}_\perp)$, is the familiar thermally smeared elastic potential. Note too that the first-order terms are equivalent to the first two terms in the work of Rose and co-workers [27–30]. A guide to this equivalence is provided at the end of the Appendix.

Using Eq. (5), the first-order wave functions, which we call scattering functions, describing thermal scattering from a single atom may be written as

$$\psi_a(\mathbf{r}_\perp) = V_{1,1}(\mathbf{r}_\perp)\phi(\mathbf{r}_\perp),$$
$$\psi_b(\mathbf{r}_\perp) = V_{1,0}(\mathbf{r}_\perp)\phi(\mathbf{r}_\perp). \quad (8)$$

Note that we have substituted a function $\phi(\mathbf{r}_\perp)$ where the derivation of Eq. (5) should strictly have the elastic wave function incident upon the atom. This is because, as we shall presently show, to a good approximation other wave functions can be used for the purpose and in so doing improve the efficiency of the calculation. Fig. 3(a) shows $V_{1,1}(\mathbf{r}_\perp)$ for a silver atom. The entire crystal consists of many atoms and with each of them we associate such a set of potentials. This is consistent with the Einstein model where each atom vibrates independently. Thus incoherence is included in two senses: each atom is treated independently and so thermal scattering from different atoms is incoherent, and, by using two wave functions per atom, the thermal scattering from a single atom is the incoherent sum of different contributions. The elastic wave field incident upon each atom in the sample will initiate mutually incoherent scattered wave functions like those above. We shall assume that these wave functions will not undergo absorption thereafter. This is comparable to the single elastic-to-inelastic scattering approximation made in most coupled channels work [33].

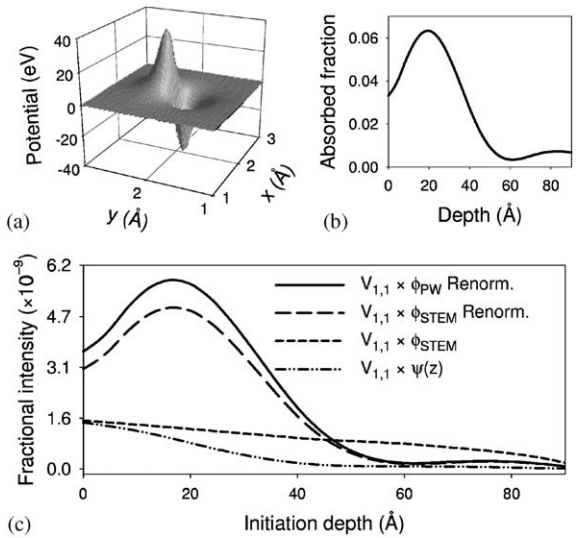

Fig. 3. (a) The $V_{1,1}(\mathbf{r}_\perp)$ potential for a silver atom [$V_{1,0}(\mathbf{r}_\perp)$ has the same form, rotated by 90°]. (b) The number of electrons absorbed in each repeat distance as a function of depth, rated as a fraction of incident flux with the aberration-balanced probe used in Fig. 2 situated atop a silver column. (c) The total EELS signal produced by the thermal channel wave functions initiated at the depth shown. The effective wave functions ϕ_{PW} and ϕ_{STEM} denote that the effective probe is a plane wave and the STEM probe at the surface, respectively, while $\psi(z)$ denotes that the effective probe is the elastic wave function at the depth of the atom. "Renorm." denotes that the results have been renormalized to force conservation of electrons.

Rose and co-workers introduce random phases such that the incoherence between thermally scattered wave functions for an individual atom, and between different atoms, can be built in. We will not take that approach but rather treat each atom independently at the outset. Anstis et al. [26] note that the number of scattering functions required for full convergence can be large. As it stands both these properties reduce the efficiency

of the algorithm. However some simplifications can be made.

Strictly, the wave function $\phi(\mathbf{r}_\perp)$ causing the excitations in Eq. (8) should be the dynamical wave function $\psi(\mathbf{r}_\perp)$. However this requires a calculation of the propagation of $\psi_a(\mathbf{r}_\perp)$ and $\psi_b(\mathbf{r}_\perp)$ for every depth since the evolution of the wave function $\psi(\mathbf{r}_\perp)$ causes it to change at each depth and thus produce different scattering functions $\psi_a(\mathbf{r}_\perp)$ and $\psi_b(\mathbf{r}_\perp)$ at each depth. However the product in Eq. (8) gives a localized function because the scattering potentials $V_{1,1}(\mathbf{r}_\perp)$ and $V_{1,0}(\mathbf{r}_\perp)$ are localized at the site of the atom. Thus not all of the dynamical wave function is required, just the portion in proximity to the scatterer. This suggests an interesting possibility: if one could use the same function $\phi(\mathbf{r}_\perp)$ for all depths, which loosely assumes that the form of the dynamical wave function close to the columns does not change significantly with depth, then one would only need to propagate $\psi_a(\mathbf{r}_\perp)$ and $\psi_b(\mathbf{r}_\perp)$ once through the crystal for each distinct atom in the unit cell, the contribution from atoms at all depths being obtainable then from various stages of this single propagation. For example, for the same $\psi_a(\mathbf{r}_\perp)$, propagation from the top of the crystal to the middle gives the same resultant wave function as would be obtained if $\psi_a(\mathbf{r}_\perp)$ was propagated starting at the middle out to the exit face. We will consider two possible forms for this general approximation to $\phi(\mathbf{r}_\perp)$: that of a plane wave and that of the incident STEM probe. The former assumes the dynamical wave function is effectively constant within the region where $V_{1,1}(\mathbf{r}_\perp)$ and $V_{1,0}(\mathbf{r}_\perp)$ are significant, the latter provides some attenuation about the atom location and may be more appropriate for tightly localized probes.

These approximations would give poor results if it were not for one further modification which moreover allows us to limit the number of scattering functions required. Eq. (8) implies an absolute scale: the product of the scattering function and the incident wave function gives the scattered wave function. However proceeding in this fashion using only two scattering functions does not conserve electron flux [and the consequences are more pronounced if $\phi(\mathbf{r}_\perp)$ is treated approximately since its normalization is not given]. In order to use just two scattering functions, the first-order terms, and yet get a better estimate for the magnitude of the contribution we renormalize the electron density in these scattered functions such that is equal to that absorbed from the elastic wave function. It is this step that puts the true dynamically evolving wave function into the calculation, even if a plane wave is used as the effective exciting function $\phi(\mathbf{r}_\perp)$, through the degree of absorption to which the true wave function is subjected.

Fig. 3(b) shows the fraction of the incident flux absorbed in one repeat distance as a function of depth with the 100 keV, aberration-balanced probe, characterized by $\Delta f = 62\,\text{Å}$, $C_s = -0.05\,\text{mm}$, $C_5 = 63\,\text{mm}$, and probe-forming semi-angle of 20 mrad, as used in the preceding figures, positioned on an atomic column in [1 0 0] Ag. Fig. 3(c) shows the total EELS signal produced by the wave functions initiated by a single atom at a given depth. The plots that do not include renormalization to the proportion of electrons absorbed are seen to give a significantly lower signal strength than those that do. We will presently show that it is the renormalized signals which give good agreement with the frozen lattice model. Similarly, provided the renormalization is performed, the correction obtained when higher order terms in Eq. (5) are included is negligible. That the first-order potential terms are antisymmetric suggests that for very fine probes it will be necessary to take higher order terms into account, however none of the probes and simulations described herein require this.

If the effective probe is a plane wave, or at least the variation of the wave function is sufficiently slow across the effective scattering potential that it may be approximated as such, then the scattered wave functions arising from equivalent atoms in equivalent cells are identical and it suffices to calculate the contribution only once for each different atom in the unit cell for the entire crystal. When this approximation is justified we can use this model to calculate STEM EELS images which account for the contribution from thermally scattered electrons very efficiently because the thermally scattered components needs only to be run once (cf. the frozen lattice model where the average over configurations must be performed

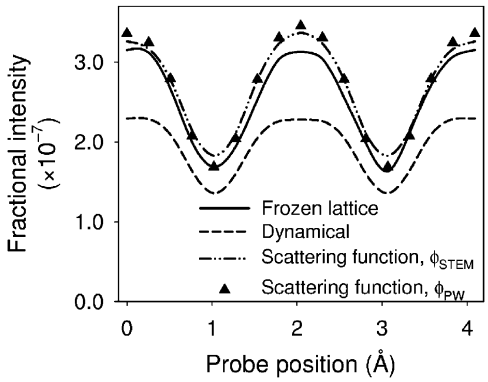

Fig. 4. Ag L-shell EELS line scans simulated with the aberration-balanced probe. The frozen lattice and dynamical simulations are provided for reference. The two approximations, ϕ being the STEM probe and ϕ being a plane wave, are seen to be in good agreement with the results of the frozen lattice model.

for each and every probe position). This is in the spirit of the "β-approximation" of Anderson et al. [34] which greatly improved the efficiency of calculating high-angle annular dark field images by an approximation to the approach of Dinges et al. [27].

The validity of these approximations is best tested through comparison with more detailed calculations. Such a comparison is presented in Fig. 4. It is seen that both approximations are in good agreement with the frozen lattice model. Taken as a correction to the absorptive model, it certainly provides an excellent indication of where the contribution from thermally scattered electrons should not be neglected.

5. Case study: Ti L-shell EELS on $SrTiO_3$

Allen et al. [2] presented a comparison between theoretical and experimental results for a line scan measurement of Ti L-shell EELS on $SrTiO_3$ with the emphasis that column-by-column spectroscopy is indeed possible, that the nature of the ionization interaction was less of a limit to resolution than the probe size with current generation equipment. It was also suggested that, for increasingly fine probes, a significant Ti L-shell EELS signal may be picked up on the Sr column as a result of the significant number of electrons thermally scattered by it. However that simulation was based on the diffuse contribution in Eq. (1) which we now believe to be inadequate for the accurate description of the contribution of thermally scattered electrons in STEM. In this section the theoretical predictions of the paper will be re-examined in light of the new models. The reader is referred to the original paper for more details about the associated experiment. We emphasize that the conclusions made there about the localization of the signal to the column and the possibility of column-by-column spectroscopic analysis still hold.

Consider three 100 keV probes. The first is aberration-free, with a probe-forming semi-angle of 37 mrad. The second is the aberration-balanced probe, with $\Delta f = 62\,\text{Å}$, $C_s = -0.05\,\text{mm}$, $C_5 = 63\,\text{mm}$, and a probe-forming semi-angle of 20 mrad, pertaining to the EELS experiment described by Allen et al. [2]. The third is aberrated, with $C_s = 0.5\,\text{mm}$ and Scherzer conditions (giving a semi-angle of 14 mrad). Calculated using an Einstein absorption model, Table 1 shows the proportion of intensity remaining in the elastic channel at a range of depths for the probes positioned on the Sr and TiO columns in $SrTiO_3$ [0 0 1]. This table shows that significant absorption occurs on both columns. Note that absorption is most significant for the finest probe, which places the greatest portion of its intensity upon the column, and is less significant for the broadest probe. The absorption is most significant on the heavy Sr column, indeed with the aberration-free probe situated on the Sr column almost half of the incident flux has been absorbed by 50 Å. It is unsurprising then that a model which treats the contribution to the EELS signal from thermally scattered electrons as proportional to the fraction of absorbed electrons will give significant signal for a probe situated on the Sr column, even if it is Ti L-shell ionization being measured. It is also easy to see why a realistic account of thermal scattering is needed: the thermal channels may contain a significant portion of the electron density.

We shall simulate EELS scans based on Ti L-shell ionization, with a detector semi-angle of

Table 1
Proportion of intensity remaining subsequent to absorption

Depth (Å)	Aberration-free probe		Aberration-balanced probe		Aberrated probe	
	Sr column	TiO column	Sr column	TiO column	Sr column	TiO column
39	0.55	0.76	0.60	0.79	0.80	0.87
78	0.34	0.58	0.46	0.67	0.68	0.78
117	0.26	0.46	0.37	0.56	0.63	0.72
156	0.22	0.38	0.35	0.50	0.58	0.66
195	0.20	0.32	0.32	0.45	0.55	0.63

20 mrad, and an energy window of 40 eV above the ionization threshold. The zone axis is [0 0 1]. The thickness is 200 Å. The line scans are taken along the [1 1 0] direction in which Sr columns alternate with TiO columns. Fig. 5 shows the cross sections calculated in the four models being discussed. The scattering function calculation, in which $\phi(\mathbf{r}_\perp)$ is approximated by the STEM probe wave function incident upon the entrance surface, is again seen to be in good agreement with the frozen lattice model. Using a plane wave for $\phi(\mathbf{r}_\perp)$ does not alter this result on the Sr columns, but gives a signal on the TiO column more similar to that of the absorptive model; the agreement between the two approximations in this case is less good than it was for silver (Fig. 4).

The difference between the scattering function and dynamical models is purely due to the additional electron density included within the scattering functions. As such we shall regard the dynamical simulation as the reference against which we judge what additional effect is introduced when the distribution of thermally scattered electrons are taken into account.

There is a notable difference in Fig. 5 between the frozen lattice simulation and the dynamical simulation at the location of the TiO column due to ionization events caused by electrons in the thermal background. Given that for the aberration-free probe about 50% of the electron density consists of thermally scattered electrons by 100 Å, the contribution from thermally scattered electrons is relatively small. This is because the thermal scattering functions do not contribute coherently. Note too that the difference is less pronounced the broader the probe, correlating well with the smaller degree of absorption occasioned by these probes (cf. Table 1).

The proportion of electrons absorbed when the probe is on the Sr column is even greater than when it is on the TiO column, and yet in absolute terms the difference between the frozen lattice and dynamical simulations is very small around the Sr column. Thus while the proportion of intensity absorbed is large, the distribution therein does not give a significant contribution to the Ti L-shell EELS signal.

The absorptive model is seen to over-estimate the thermal contribution to the TiO column and greatly over-estimate the thermal contribution to the Sr column relative to the frozen lattice model, though the discrepancy decreases for broader probes. That said, the difference between simulations with and without accounting for the distribution of thermally scattered electrons is notable about the TiO column: thermal scattering is important and there will be a need in quantitative work for modelling this detail.

As a final note, the shapes of the plots are also of some interest. In Fig. 1 we saw that, for the M-shell plots, the signal strength at the column location was lower than that with the probe slightly displaced because of the degree of absorption. Table 1 shows that the absorption on the TiO column is greater for the finer aberration-free probe. Why then is it the broader probe which has the volcano-like profile? This is a nontrivial question because the signal results from a complex interplay of many factors: the nonlocal nature of the potential, the absorption by thermal scattering, and the dynamical channelling of the probe. Investigations of the per slice contribution, a calculation

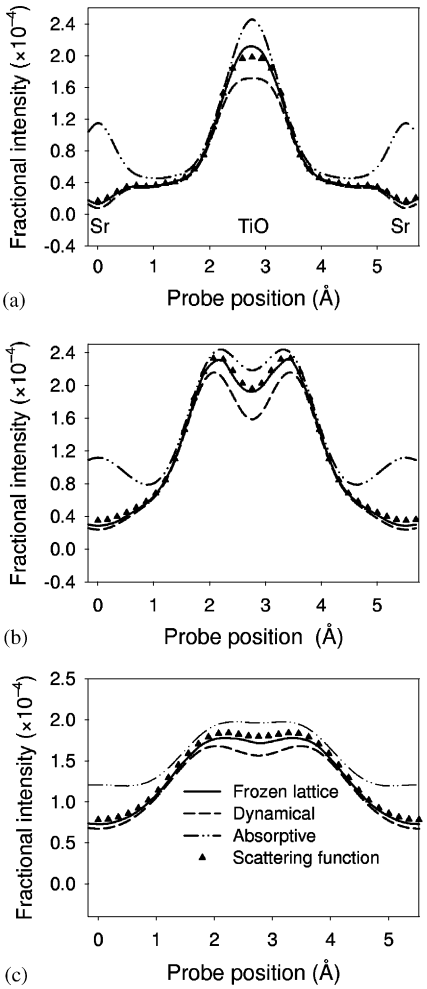

Fig. 5. Ti L-shell EELS images in $SrTiO_3$ using (a) the aberration-free probe, (b) the aberration-balanced probe, and (c) the aberrated probe. The solid line is calculated from Eq. (4), the result of the frozen lattice MDFF synthesis. The dashed line is calculated in the dynamical model [i.e. using only the first term in Eq. (1)], while the dash-dot line is calculated in the absorptive model [i.e. using both terms in Eq. (1)]. The triangles are calculated from the scattering function model with $\phi(\mathbf{r}_\perp)$ approximated by the STEM probe wave function incident upon the entrance surface.

similar to those of Fig. 1(c) and (d), show that for probes on the TiO column the fine probe gives little oscillatory behaviour but rather a trend of signal decreasing with thickness while for the broader probe the per slice contribution oscillates with depth. In the latter case the oscillations are much less pronounced with slight displacements off column. Thus the volcano-type profile for the aberration-balanced probe arises largely because the signal on column is reduced due to the oscillatory behaviour in comparison to that for slight displacements. By contrast, the finer probe, which has a larger aperture and therefore higher transverse momentum components, is moderately attenuated by the absorption when on the column, but this does not lead to dissipation of the intensity near the column so readily as when this probe is displaced off the column in which case it spreads out considerably.

6. Conclusion

For the purposes of designing experiments or makings qualitative interpretations, the combination of the MDFF approach with the dynamical model provides an efficient means of simulating EELS images in STEM. Indeed for moderate probe sizes, very thin crystals, crystals composed entirely of light atoms and other such cases in which the degree of thermal absorption is small, the correction over the dynamical contribution obtained by a detailed accounting for thermal scattering is minor. However for cases where there is a significant degree of absorption, which may result from strongly scattering samples or from finely focused probes, more quantitative work will require an accounting for the role of thermal scattering. It has been seen that the previously presented diffuse model is inadequate for this purpose; the methods presented here represent a considerable improvement.

The complexity and computation time involved in the frozen lattice model (Eq. (4)), is appreciable. As experimental equipment improves, and the comparison between theory and experiment becomes more quantitative, calculations of this detail will be a vital adjunct to image interpretation. At present it seems more useful to explore where complications in direct image interpretation may arise. The scattering function approach constitutes one such approximate method allowing the contribution to EELS images arising from thermal scattering to be estimated. When $\phi(\mathbf{r}_\perp)$ in Eq. (8) is

justifiably approximated by a plane wave, this approach can be made very efficient.

While we have focused on core-loss spectroscopy, it should be noted that the combination of the MDFF model with means to handle the thermally scattered electrons can be applied to any form of inelastic scattering for which the MDFFs are known. The simulation of energy dispersive X-ray spectroscopy is one such example.

In summary, the increasing interest in STEM EELS as an experimental technique will necessitate the detailed modelling of the distribution of electrons scattering from the crystal undergoing thermal motion. The techniques presented, the synthesis of methods for calculating the realistic distributions of thermally scattered electrons with the MDFF method for calculating inelastic images, provide a means of doing this.

Acknowledgements

The authors would like to thank the referees for many helpful suggestions. M.P. Oxley and L.J. Allen acknowledge support by the Australian Research Council. S.J. Pennycook acknowledges support by the Laboratory Directed Research and Development Program of ORNL, managed by UT-Battelle, LLC, for the US Department of Energy under Contract no. DE-AC05-00OR22725.

Appendix. Derivation of the scattering functions

We reconsider the derivation by Hall and Hirsch [31] of the effect on the scattering of electrons due to the thermal vibration of the atoms. We consider a single, isolated atom, the position of which is described by an average position $\mathbf{R}_0$ and the time-dependent displacement $\mathbf{u}(t)$:

$$\mathbf{R}(t) = \mathbf{R}_0 + \mathbf{u}(t). \tag{A.1}$$

Suppose the incident wave function can be written in the form

$$\psi(\mathbf{r}) \equiv \psi(\mathbf{r}_\perp, z) = \sum_{\mathbf{g}} C_{\mathbf{g}} \exp[2\pi \mathrm{i}(\mathbf{k}_0 + \mathbf{g}) \cdot \mathbf{r}], \tag{A.2}$$

where $\mathbf{k}_0$ is the wave vector and $\mathbf{g}$ denotes a reciprocal space vector in the plane perpendicular to the optical axis, though for a single atom the mesh on which $\mathbf{g}$ lies is not strictly discrete. We seek to express the intensity scattered to the vector $\mathbf{s} = \mathbf{k} - \mathbf{k}_0$. In what follows we shall make use of the flat Ewald sphere approximation to assert that $\mathbf{s}$ will lie in the zero order Laue zone. Using the kinematic approximation, and following the reasoning of Hall and Hirsch [31], the intensity scattered to $\mathbf{s}$ is

$$\begin{aligned} I(\mathbf{s}) &= \left\{ \sum_{\mathbf{g}} C_{\mathbf{g}} f_{\mathbf{s}-\mathbf{g}} \exp[-2\pi \mathrm{i}(\mathbf{s}-\mathbf{g}) \cdot \mathbf{R}] \right\} \\ &\quad \times \left\{ \sum_{\mathbf{h}} C_{\mathbf{h}} f_{\mathbf{s}-\mathbf{h}} \exp[-2\pi \mathrm{i}(\mathbf{s}-\mathbf{h}) \cdot \mathbf{R}] \right\}^* \\ &= \sum_{\mathbf{g},\mathbf{h}} C_{\mathbf{g}} C_{\mathbf{h}}^* f_{\mathbf{s}-\mathbf{g}} f_{\mathbf{s}-\mathbf{h}}^* \exp[2\pi \mathrm{i}(\mathbf{h}-\mathbf{g}) \cdot \mathbf{R}]. \end{aligned} \tag{A.3}$$

Taking the thermal average over positions of the atom, assuming an Einstein model, we write

$$\langle I(\mathbf{s}) \rangle = \sum_{\mathbf{g},\mathbf{h}} C_{\mathbf{g}} C_{\mathbf{h}}^* f_{\mathbf{s}-\mathbf{g}} f_{\mathbf{s}-\mathbf{h}}^* \langle \exp[-2\pi \mathrm{i}(\mathbf{h}-\mathbf{g}) \cdot \mathbf{R}] \rangle. \tag{A.4}$$

Using Eq. (A.1) this becomes

$$\begin{aligned} \langle I(\mathbf{s}) \rangle = &\sum_{\mathbf{g},\mathbf{h}} C_{\mathbf{g}} C_{\mathbf{h}}^* f_{\mathbf{s}-\mathbf{g}} f_{\mathbf{s}-\mathbf{h}}^* \exp[-2\pi \mathrm{i}(\mathbf{h}-\mathbf{g}) \cdot \mathbf{R}_0] \\ &\times \langle \exp[-2\pi \mathrm{i}(\mathbf{h}-\mathbf{g}) \cdot \mathbf{u}(t)] \rangle. \end{aligned} \tag{A.5}$$

Using the harmonic oscillator or Einstein model for the single atom, the thermal average obeys the rule $\langle \exp(A) \rangle = \exp(\frac{1}{2}\langle A^2 \rangle)$ [35]. Thus the previous equation may be re-written as

$$\begin{aligned} &\langle \exp[-2\pi \mathrm{i}(\mathbf{h}-\mathbf{g}) \cdot \mathbf{u}(t)] \rangle \\ &\quad = \exp\{-2\pi^2 \langle [(\mathbf{h}-\mathbf{g}) \cdot \mathbf{u}(t)]^2 \rangle\} \\ &\quad \equiv \exp[-2\pi^2 (\mathbf{h}-\mathbf{g})^2 \langle u_p^2 \rangle], \end{aligned} \tag{A.6}$$

where $\langle u_p^2 \rangle$ denotes the projected mean square vibrational amplitude. The last term in the previous equation may be expanded as

$$\begin{aligned} &\exp[-2\pi^2 (\mathbf{h}-\mathbf{g})^2 \langle u_p^2(t) \rangle] \\ &\quad = \exp[-2\pi^2 (\mathbf{s}-\mathbf{g})^2 \langle u_p^2(t) \rangle] \exp[-2\pi^2 (\mathbf{s}-\mathbf{h})^2 \\ &\qquad \times \langle u_p^2(t) \rangle] \exp[4\pi^2 (\mathbf{s}-\mathbf{g}) \cdot (\mathbf{s}-\mathbf{h}) \langle u_p^2(t) \rangle] \\ &\quad \equiv \exp[-M(\mathbf{s}-\mathbf{g})] \exp[-M(\mathbf{s}-\mathbf{h})] \\ &\qquad \times \exp[4\pi^2 (\mathbf{s}-\mathbf{g}) \cdot (\mathbf{s}-\mathbf{h}) \langle u_p^2(t) \rangle], \end{aligned} \tag{A.7}$$

where we have introduced the Debye–Waller factor $M(\mathbf{g}) = 2\pi^2\mathbf{g}^2\langle u_p^2(t)\rangle$. Now consider the last exponential term in Eq. (A.7). Consider the Taylor expansion

$$\begin{aligned}\exp(c\mathbf{p}\cdot\mathbf{q}) &= \sum_{n=0}^{\infty}\frac{c^n(\mathbf{p}\cdot\mathbf{q})^n}{n!} = \sum_{n=0}^{\infty}\frac{c^n}{n!}(p_xq_x+p_yq_y)^n \\ &= \sum_{n=0}^{\infty}\sum_{k=0}^{n}\frac{c^n}{(n-k)!k!}p_x^kp_y^{n-k}q_x^kq_y^{n-k}, \end{aligned} \tag{A.8}$$

where in the final step we have used the binomial theorem. Identifying c with $4\pi^2\langle u_p^2(t)\rangle$, $\mathbf{p}$ with $\mathbf{s}-\mathbf{g}$, and $\mathbf{q}$ with $\mathbf{s}-\mathbf{h}$ we may combine Eqs. (A.6)–(A.8), motivated by the approach of Anstis and co-workers [25,26], to re-write (A.5) as

$$\begin{aligned}\langle I(\mathbf{s})\rangle &= \sum_{\mathbf{g},\mathbf{h}} C_{\mathbf{g}}C_{\mathbf{h}}^*\{f_{\mathbf{s}-\mathbf{g}}\exp[-M(\mathbf{s}-\mathbf{g})]\}\{f_{\mathbf{s}-\mathbf{h}}^* \\ &\quad\times\exp[-M(\mathbf{s}-\mathbf{h})]\}\sum_{n=0}^{\infty}\sum_{k=0}^{n}\frac{[4\pi^2\langle u_p^2\rangle]^n}{(n-k)!k!} \\ &\quad\times(\mathbf{s}-\mathbf{g})_x^k(\mathbf{s}-\mathbf{g})_y^{n-k}(\mathbf{s}-\mathbf{h})_x^k(\mathbf{s}-\mathbf{h})_y^{n-k} \\ &\quad\times\exp[-2\pi\mathrm{i}(\mathbf{h}-\mathbf{g})\cdot\mathbf{R}_0] \\ &= \sum_{n=0}^{\infty}\sum_{k=0}^{n}\frac{[4\pi^2\langle u_p^2\rangle]^n}{(n-k)!k!}\left\{\sum_{\mathbf{g}} C_{\mathbf{g}}f_{\mathbf{s}-\mathbf{g}}\right. \\ &\quad\times\exp[-M(\mathbf{s}-\mathbf{g})](\mathbf{s}-\mathbf{g})_x^k(\mathbf{s}-\mathbf{g})_y^{n-k} \\ &\quad\left.\times\exp[-2\pi\mathrm{i}(\mathbf{s}-\mathbf{g})\cdot\mathbf{R}_0]\right\}\left\{\sum_{\mathbf{h}} C_{\mathbf{h}}f_{\mathbf{s}-\mathbf{h}}\right. \\ &\quad\times\exp[-M(\mathbf{s}-\mathbf{h})](\mathbf{s}-\mathbf{h})_x^k(\mathbf{s}-\mathbf{h})_y^{n-k} \\ &\quad\left.\times\exp[-2\pi\mathrm{i}(\mathbf{s}-\mathbf{h})\cdot\mathbf{R}_0]\right\}^* \\ &\equiv \sum_{n=0}^{\infty}\sum_{k=0}^{n}|\psi_{n,k}(\mathbf{s})|^2, \end{aligned} \tag{A.9}$$

where

$$\begin{aligned}\psi_{n,k}(\mathbf{s}) &= \sqrt{\frac{[4\pi^2\langle u_p^2\rangle]^n}{(n-k)!k!}}\sum_{\mathbf{g}} C_{\mathbf{g}}f_{\mathbf{s}-\mathbf{g}}\exp[-M(\mathbf{s}-\mathbf{g})] \\ &\quad\times(\mathbf{s}-\mathbf{g})_x^k(\mathbf{s}-\mathbf{g})_y^{n-k}\exp[-2\pi\mathrm{i}(\mathbf{s}-\mathbf{g})\cdot\mathbf{R}_0] \\ &\equiv A_{n,k}\sum_{\mathbf{g}} C_{\mathbf{g}}f_{\mathbf{s}-\mathbf{g}}\exp[-M(\mathbf{s}-\mathbf{g})](\mathbf{s}-\mathbf{g})_x^k \\ &\quad\times(\mathbf{s}-\mathbf{g})_y^{n-k}\exp[-2\pi\mathrm{i}(\mathbf{s}-\mathbf{g})\cdot\mathbf{R}_0] \end{aligned} \tag{A.10}$$

and we have defined

$$A_{n,k} = \sqrt{\frac{[4\pi^2\langle u_p^2\rangle]^n}{(n-k)!k!}}. \tag{A.11}$$

Using the convolution theorem we may write this as

$$\psi_{n,k}(\mathbf{s}) = \mathscr{F}\{V_{n,k}(\mathbf{r}_\perp)\psi(\mathbf{r}_\perp)\}, \tag{A.12}$$

where $\mathscr{F}$ denotes a 2D Fourier transform, we have made use of Eq. (A.2), and defined

$$\begin{aligned}V_{n,k}(\mathbf{r}_\perp) &\equiv A_{n,k}\sum_{\mathbf{h}} f_{\mathbf{h}}\exp[-M(\mathbf{h})]h_x^kh_y^{n-k} \\ &\quad\times\exp[2\pi\mathrm{i}\mathbf{h}\cdot(\mathbf{r}_\perp-\mathbf{R}_0)]. \end{aligned} \tag{A.13}$$

In summary, the intensity may be written as

$$\langle I(\mathbf{s})\rangle = \sum_{n=0}^{\infty}\sum_{k=0}^{n}|\mathscr{F}\{V_{n,k}(\mathbf{r}_\perp)\psi(\mathbf{r}_\perp)\}|^2. \tag{A.14}$$

Note that the zeroth-order term

$$\begin{aligned}V_{0,0}(\mathbf{r}_\perp) &= \sum_{\mathbf{h}} f_{\mathbf{h}}\exp[-M(\mathbf{h})] \\ &\quad\times\exp[2\pi\mathrm{i}\mathbf{h}\cdot(\mathbf{r}_\perp-\mathbf{R}_0)] \end{aligned} \tag{A.15}$$

is simply the expression for the thermally smeared elastic potential of an atom. Thus the first term in the series of Eq. (A.14) is simply the scattering distribution due to elastic scattering of a single atom in the first Born approximation.

Using Eq. (A.13), first-order terms may be written as

$$\begin{aligned}V_{1,1}(\mathbf{r}_\perp) &= A_{1,1}\sum_{\mathbf{h}} f_{\mathbf{h}}\exp[-M(\mathbf{h})]h_x \\ &\quad\times\exp[2\pi\mathrm{i}\mathbf{h}\cdot(\mathbf{r}_\perp-\mathbf{R}_0)], \\ V_{1,0}(\mathbf{r}_\perp) &= A_{1,0}\sum_{\mathbf{h}} f_{\mathbf{h}}\exp[-M(\mathbf{h})]h_y \\ &\quad\times\exp[2\pi\mathrm{i}\mathbf{h}\cdot(\mathbf{r}_\perp-\mathbf{R}_0)]. \end{aligned} \tag{A.16}$$

Using an analytic parameterization for the electron scattering factors of the form

$$f(\mathbf{g}) = \sum_{v} A_v\exp[-B_v\mathbf{g}^2/4], \tag{A.17}$$

such as that of Peng et al. [36], and converting the discrete sum in Eq. (A.16) to an integral as appropriate for the treatment of a single atom,

it may be shown that

$$V_{1,1}(\mathbf{r}_\perp) = \mathrm{i}16\pi^2 A_{1,1} r_x \sum_v \frac{A_v}{[B_v + 4M]^2} \times \exp\left[-\frac{4\pi^2 r_\perp^2}{B_v + 4M}\right],$$

$$V_{1,0}(\mathbf{r}_\perp) = \mathrm{i}16\pi^2 A_{1,0} r_y \sum_v \frac{A_v}{[B_v + 4M]^2} \times \exp\left[-\frac{4\pi^2 r_\perp^2}{B_v + 4M}\right]. \quad \text{(A.18)}$$

These equations are equivalent to the effective transmission functions for thermal scattering introduced by Dinges et al. [27]. We have introduced this parameterization to show this equivalence, but simulations in this paper were based upon the parameterization of Waasmaier and Kirfel [37].

References

[1] N. Dellby, O.L. Krivanek, P.D. Nellist, P.E. Batson, A.R. Lupini, J. Electron Microsc. 50 (2001) 177.
[2] L.J. Allen, S.D. Findlay, A.R. Lupini, M.P. Oxley, S.J. Pennycook, Phys. Rev. Lett. 91 (2003) 105503.
[3] A.R. Lupini, S.J. Pennycook, Ultramicroscopy 96 (2003) 313.
[4] M. Varela, S.D. Findlay, A.R. Lupini, H.M. Christen, A.Y. Borisevich, N. Dellby, O.L. Krivanek, P.D. Nellist, M.P. Oxley, L.J. Allen, S.J. Pennycook, Phys. Rev. Lett. 92 (2004) 095502.
[5] V.W. Maslen, C.J. Rossouw, Philos. Mag. A 49 (1984) 735.
[6] C.J. Rossouw, V.W. Maslen, Philos. Mag. A 49 (1984) 743.
[7] H. Kohl, H. Rose, Adv. Imag. Electron Phys. 65 (1985) 173.
[8] D.K. Saldin, P. Rez, Philos. Mag. B 55 (1987) 481.
[9] L.J. Allen, T.W. Josefsson, Phys. Rev. B 52 (1995) 3184.
[10] M.P. Oxley, L.J. Allen, Phys. Rev. B 57 (1998) 3273.
[11] L.J. Allen, C.J. Rossouw, Phys. Rev. B 47 (1993) 2446.
[12] L.J. Allen, Ultramicroscopy 48 (1993) 97.
[13] T.W. Josefsson, L.J. Allen, Phys. Rev. B 53 (1996) 2277.
[14] M.P. Oxley, L.J. Allen, C.J. Rossouw, Ultramicroscopy 80 (1999) 109.
[15] P. Schattschneider, M. Nelhiebel, H. Souchay, B. Jouffrey, Micron 31 (2000) 333.
[16] L.J. Allen, S.D. Findlay, M.P. Oxley, C.J. Rossouw, Ultramicroscopy 96 (2003) 47.
[17] S.D. Findlay, L.J. Allen, M.P. Oxley, C.J. Rossouw, Ultramicroscopy 96 (2003) 65.
[18] C.J. Rossouw, L.J. Allen, S.D. Findlay, M.P. Oxley, Ultramicroscopy 96 (2003) 299.
[19] S. Hillyard, R.F. Loane, J. Silcox, Ultramicroscopy 49 (1993) 14.
[20] R.F. Loane, P. Xu, J. Silcox, Ultramicroscopy 40 (1992) 121.
[21] R.F. Loane, P. Xu, J. Silcox, Acta Crystallogr. A 47 (1991) 267.
[22] E.J. Kirkland, Advanced Computing in Electron Microscopy, Plenum Press, New York, 1998.
[23] C. Dwyer, J. Etheridge, Ultramicroscopy 96 (2003) 343.
[24] Z.L. Wang, Elastic and Inelastic Scattering in Electron Diffraction and Imaging, Plenum Press, New York, London, 1995.
[25] G.R. Anstis, J. Microsc. 194 (1999) 105.
[26] G.R. Anstis, S.C. Anderson, C.R. Birkeland, D.J.H. Cockayne, Fifteenth Pfefferkorn Conference, Silver Bay, New York, 1996, unpublished proceedings.
[27] C. Dinges, A. Berger, H. Rose, Ultramicroscopy 60 (1995) 49.
[28] P. Hartel, H. Rose, C. Dinges, Ultramicroscopy 63 (1996) 93.
[29] H. Müller, H. Rose, P. Schorsch, J. Microsc. 190 (1998) 73.
[30] C. Dinges, H. Rose, Scanning Microsc. 11 (1997) 277.
[31] C.R. Hall, P.B. Hirsch, Proc. Roy. Soc. London A 286 (1965) 158.
[32] G.R. Anstis, Acta Crystallogr. A 52 (1996) 450.
[33] W. Coene, D. Van Dyck, Ultramicroscopy 33 (1990) 261.
[34] S.C. Anderson, C.R. Birkeland, G.R. Anstis, D.J.H. Cockayne, Ultramicroscopy 69 (1997) 83.
[35] B.T.M. Willis, A.W. Pryor, Thermal Vibrations in Crystallography, Cambridge University Press, London, New York, 1975.
[36] L.-M. Peng, G. Ren, S.L. Dudarev, M.J. Whelan, Acta Crystallogr. A 52 (1996) 257.
[37] D. Waasmaier, A. Kirfel, Acta Crystallogr. A 51 (1995) 416.